Journal of Materials Chemistry A

Accepted Manuscript

ROYAL SOCIETY OF CHEMISTRY

www.rsc.org/materialsA

Journal Name

RSCPublishing

ARTICLE

Enhanced thermal conductivity of PEG/diatomite shape-stabilized phase change materials with Ag nanoparticles for thermal energy storage

Tingting Qian, Jinhong Li,† Xin Min, Weimin Guan, Yong Deng, Lei Ning,

Cite this: DOI: 10.1039/x0xx00000x

Received 00th January 2012,
Accepted 00th January 2012

DOI: 10.1039/x0xx00000x

www.rsc.org/

Ag nanoparticle (AgNP) is a promising additive because it can enhance the thermal conductivity of organic phase change materials. In this paper, a series of high thermal-conductive shape-stabilized phase change materials (ss-PCMs) were tailored by blending PEG with AgNP-decorated diatomite. In order to enlarge its pore size and specific surface area and make it a suitable PEG carrier, the effect of alkali leaching on the microstructure of diatomite was studied. While PEG melted during phase transformation, the maximum load of PEG could reach 63 wt.%, which was 31% higher than that of the raw diatomite. Spherical-shaped crystalline AgNPs with the diameter range of 3~10 nm were uniformly decorated onto the diatomite. The XPS result of this material proved that the valence state of silver in PEG/diatomite PCM was mainly zero. The phase change enthalpy of PEG/diatomite/Ag PCM reached 111.3 J/g, and the thermal conductivity of PEG/diatomite PCM containing 7.2 wt.% Ag was 0.82 $W \cdot m^{-1} \cdot K^{-1}$, which was 127% higher than that of PEG/diatomite composite. The reduced melting and freezing periods indirectly proved that the heat transfer in the composite material during the heat storage and release process was enhanced through the thermal conductivity improvement. The composite PCM was stable in terms of thermal and chemical manners even after 200 cycles of melting and freezing. It was indicated that the resulting composite PCMs were promising candidate materials for building applications due to its large latent heat, suitable phase change temperature, excellent chemical compatibility, improved supercooling extent, and high thermal stability.

Introduction

Sustainable and renewable energy like solar energy has been a factor of vital importance since the energy crisis in the 1970s. Thermal energy storage (TES) including sensible heat storage and latent heat storage has turned out to be a most perspective and low-cost technique for energy conservation efficiency enhancement,[1] which also in turn alleviates the environmental impact related to energy consumption. The technique actually provides a constructive solution for correcting the common big imbalance between the energy supply and demand.[2,3] Among TES methods, latent heat energy storage realized using a phase change material (PCM) is found to be the most effective technique because of its high energy storage density and isothermal characteristics.[4] Compared to the sensible heat storage method, the latent heat storage method can realize the much higher storage density with a smaller temperature difference between storing and releasing heat.[5]

PCM is a sort of functional materials allowing the cycle of heat storage and release from its melting to solidification within a slight temperature change.[6] In the past few years, PCMs have attracted wide attention from the fields of solar thermal energy application, peak load shifting, and thermal management system.[7,8] PCMs are usually categorized into organic and inorganic materials according to their components. Organic PCMs are widely used due to their high latent heat density, suitable phase transition temperature, smaller temperature swings, stable physical and chemical properties for long-term usage, and competitive price. Generally, organic PCMs mainly include paraffin waxes (or n-alkanes), polyethylene glycols (PEGs), and fatty acids.[9,10] PEG was the most widely studied PCM.[11] However, there are still several insurmountable defects for applications of PEG PCMs in traditional manners. For example, it is difficult to handle the materials during the phase change from solid to liquid. Moreover, low thermal conductivity and high degree of supercooling lead to the hysteresis of thermal response. Such drawbacks may degrade the performance of energy storage and thermal regulation during the melting and freezing cycles and restrict their final applications.[12,13]

The above problems are expected to be addressed with a packaging technology, such as encapsulation or shape stabilization, to develop shape-stabilized PCMs either in a liquid or solid state. Honestly, encapsulating PCMs into inertial polymeric or inorganic materials seems to be a useful way to isolate them from surrounding materials.[14,15] However, the laborious encapsulation process of PCMs often increases the synthesis cost. Moreover, there are still some disadvantages, such as poor thermal and chemical stability, flammability, and low thermal conductivity for microcapsules. In recent years, shape-stabilized PCMs (ss-PCMs) have become the main focus of scientific studies because ss-PCMs adopt good

thermal-conductive supporting materials which can maintain the solid shape even when the temperature is more than the melting point of PCM itself.[16,17,18] It has been proved that this method is the most effective approach to resolve the leakage and low thermal conductivity problems of organic PCMs.

Now, the indoor comfort requirement of living environment is increasing. In this case, the idea of improving thermal comfort of light weight buildings by integrating PCMs into the building structures has been studied.[19,20] Hence, numerous ss-PCMs have been reported by incorporating PCM into porous or layered silicate building materials, including perlite,[21,22] vermiculite,[23,24] diatomite,[11, 24, 25] bentonite,[26,27] montmorillonite,[28] atapulgite,[29] kaolin,[30,31,32] opal,[33] and halloysite.[34] Table 1 summarizes the thermal properties of various composite ss-PCMs which utilize mineral construction materials as supporting materials. From Table 1, we observed that those ss-PCMs prepared with diatomite as supporting material own the maximum PCM adsorption, the greatest energy-storing density, and the highest thermal conductivity. Diatomite, a type of natural amorphous siliceous mineral from geological deposits, possesses a variety of unique properties including the highly porous structure (80–90%), excellent absorption capacity, low density, chemical inertness, and relatively low price.[35] Moreover, confining PEG inside diatomite pores greatly reduces the flammability risk of PEG at the high temperature because the inflammable diatomite can act as fire protection shell for PEG.[11,12,13] With these advantages, diatomite can be seen as a sort of feasible low-weight carrier material of PCMs for energy storage in buildings.

Table 1 Comparison of the shape-stabilized composite PCMs based on building materials in literature

PCM	Supporting Material	Method	Max. Ratio	Melting Process		Solidifying Process		Thermal conductivity ($W \cdot m^{-1} \cdot K^{-1}$)	Ref.
				H_M (J/g)	T_M (^oC)	Hs (J/g)	T_S (^oC)		
Lauric/ stearic acid	Perlite	Vacuum impregnation	43.5%	131.3	33	------	------	------	[21]
Capric/ myristic acid	Perlite	Vacuum impregnation	55.0%	85.40	21.70	89.75	20.70	0.048	[22]
Capric/ myristic acid	Vermiculite	Vacuum impregnation	20.0%	27.46	19.8	31.42	17.1	0.065	[23]
galactitol hexa myristate	Vermiculite	Vacuum impregnation	55.0%	96.21	45.86	92.46	44.63	0.14	[24]
galactitol hexa myristate	Diatomite	Vacuum impregnation	52.0%	83.75	44.90	81.13	44.26	0.19	[24]
PEG1000	Diatomite	Vacuum impregnation	50.0%	87.09	27.7	82.22	32.2	0.32	[11]
Paraffin	Diatomite	Fusion adsorption	61.0%	89.54	33.04	89.80	52.43	------	[25]
Paraffin	Bentonite	Solution intercalation	44.4%	39.03	41.7	39.84	43.4	------	[26]
Myristic acid	Bentonite	Vacuum impregnation	50.0%	54.5	53.2	56.5	49.4	------	[27]
RT20	Montmorill-onite	Fusion adsorption	40.0%	53.6	24.2	------	------	------	[28]
Capric/ almitic acid	Atapulgite	Vacuum impregnation	35.0%	48.2	21.71	------	------	------	[29]
Lauric acid	Kaolinite	Solution intercalation	48.0%	72.5	43.7	70.9	39.3	0.101	[30]
Stearic acid	Kaolin	Vacuum impregnation	39.0%	66.30	53.28	65.60	52.70	------	[31]
Lauryl alcohol	Kaolin	Vacuum impregnation	24.0%	48.08	19.14	------	------	------	[32]
Paraffin blends	Opal	Fusion adsorption	39.0%	49.05	32.82	48.38	47.25	------	[33]
Capric acid	Halloysite	Solution intercalation	60.0%	75.52	29.34	------	------	------	[34]

However, diatomite has its disadvantage that the pores of raw materials are blocked by several types of impurities, thereby reducing its porosity and commercial applicability. Although the leakage and low thermal conductivity problems are usually circumvented by introducing shape stabilization support, this is inevitably lead to the reduction in energy storage density. In order to enhance the thermal storage capacity, considerable efforts have been devoted to the development of novel ss-PCMs with high PCM load.[25]. For diatomite, although numerous methods have been used to increase its porosity and enlarge its specific surface area, such as scrubbing, calcination, acid leaching, high-speed shear, and ultrasonication,[36,37] modified diatomite-supported composite PCMs has been seldom reported. The reason may be that these methods lead to the structure destructing, inefficiency, and high cost.[38] It is necessary to develop a cheap, easy-to-handle, and eco-friendly method of diatomite modification. In the paper, we significantly enhanced the PEG adsorption capability with a facile alkali-leaching method.

Although the thermal conductivity of diatomite-based ss-PCM has been improved significantly,[12] the result is still too low. Heat transfer enhancement techniques are still required. Great efforts have been made to improve the thermal conductivity of organic PCMs.[39] The

mostly reported method is to disperse highly conductive particles into PCMs.[40,41,42,43,44] For instance, Wang et al.[45] added β-aluminum nitride (β-AlN) into the PEG/silica composite PCM and the thermal conductivity of the products was changed from 0.3847 to 0.7661 $W \cdot m^{-1} \cdot K^{-1}$ when the mass ratio of β-AlN was increased from 5% to 30%. Although the thermal conductivity of ss-PCMs could be improved in this way, it was quite difficult to achieve effective dispersion with additive particles, especially nanoparticles, due to the high surface energy and large surface area. Doping nanoparticles by in situ reduction of metal salt solution is an effective approach to improve the dispersion performance.[41] Ag nanoparticle (AgNP) is a most promising additive due to its high conductivity (429 $W \cdot m^{-1} \cdot K^{-1}$) and can enhance the thermal conductivity of organic phase change materials. In our study, AgNPs were first reported to be decorated on the diatomite to form a novel high thermal-conductive supporting material.

In our study, raw diatomite was firstly treated by alkali-leaching method to make it more suitable for acting as PEG carrier. Besides, our study capitalized on the high thermal conductivity of AgNPs. AgNPs-decorated diatomite was obtained by chemical reduction of silver nitrate. Finally, a high thermal-conductive ss-PCM was prepared by blending PEG with diatomite and AgNPs. Scanning electron microscope (SEM), high-resolution transmission electron microscope (HRTEM), Energy Dispersive X-ray Spectroscopies (EDS), N_2 adsorption-desorption isotherms, Fourier transformation infrared spectroscope (FT-IR), X-ray diffractometer (XRD) and X-ray photoelectron spectroscopy (XPS), differential scanning calorimetry (DSC), thermal gain analysis (TGA) and a hot disk thermal constants analyzer were used for characterization. The prepared PEG/diatomite/Ag (PEG/DtAg) composite PCM is a prospective candidate for the application in building envelopes in hot summer when the temperature is often as high as 50~70 °C.

Experimental

Modification of diatomite with AgNPs

The raw diatomite samples used in the experiments were obtained from Changbai Mountain Co., Ltd. The raw diatomite (denoted as RD) was well purified to improve its PEG adsorption capacity. Fig. 1(a) illustrates the schematic process for the AgNPs modification. From Fig. 1(a), firstly, diatomite particles were thermally treated at 400 °C for 2 h. Then, the obtained powder was processed through an acid-leaching process in 20 wt.% H_2SO_4 solution at 70 °C for 2 h (denoted as RD-H). Thirdly, the resulting diatomite powder was immersed in the sufficient amount of 5 wt.% sodium hydroxide solution at 80 °C for 5 min (denoted as RD-N). All the detailed laboratory procedures and experiments were given in the *Supporting Information*.

The AgNPs-decorated diatomite particles were well designed by the chemical reduction of silver nitrate via a simple hydrothermal process. A typical procedure was composed of the following steps. In Step 1, 1 g of the purified diatomite powder was dispersed in 30 mL aqueous solution with a high frequency ultrasonicator for 1 h. In Step 2, to obtain this pale gray diatomite suspension, the appropriate quantity of silver nitrate dissolved in distilled water was mixed dropwise under continuous stirring for 1 h. In Step 3, 6 mmol ascorbic acid and 45 mmol urea dissolved in distilled water was then subsequently added into the solution obtained above. In Step 4, the mixture was transferred to a Teflon-lined autoclave and then heated at 110 °C for 10 h. After cooling to the room temperature, the resultant product was separated centrifugally for 3 times, washed with water, and dried in a vacuum oven at 60 °C for 12 h to yield the required AgNPs-decorated diatomite powder (denoted as DtAg). The mass ratio of Ag in the DtAg sample was determined to be as high as 7.2 wt.%.

Preparation of PEG/DtAg composite PCMs

PEG (Mw=4000) PCM used was purchased from Beijing Chemical Reagent Co., Ltd. The latent heat of PEG was 164.6 J/g at the freezing temperature of 38.5 °C and 180.3 J/g at the melting temperature of 60.51 °C. The shape-stabilized composite PCM was prepared using vacuum impregnation, as shown in Fig. 1(b). The detailed operation procedures were also given in the *Supporting Information*. In this way, PEG was impregnated with different mass ratios (30~63%). Finally, PEG/DtAg ss-PCMs were obtained. Further characterization technologies were also summarized in the *Supporting Information*.

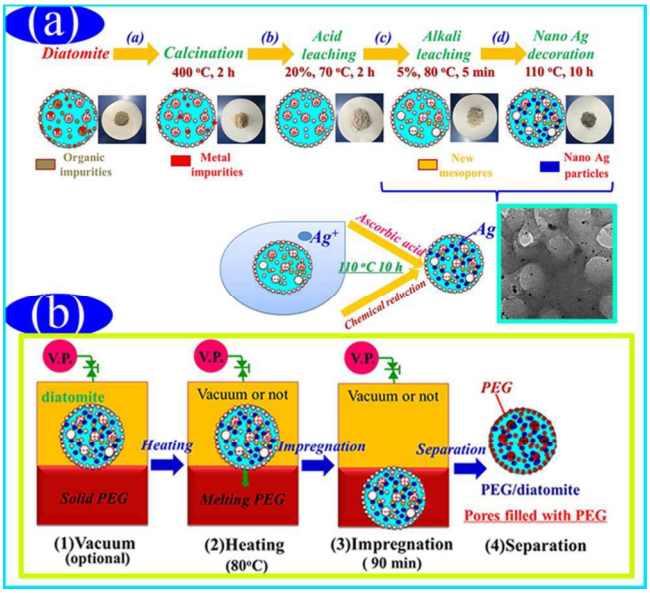

Fig. 1. (a) Schematic routes for the preparation of AgNPs-decorated diatomite powder; (b) image of vacuum impregnation treatment for preparing phase change composites (VP: vacuum pump).

Results and discussion

Characterization of AgNPs-decorated diatomite

SEM and EDS analysis. Fig. 2 shows the microstructures of raw diatomite, purified diatomite, and AgNPs-decorated diatomite powders. In Fig. 2(a), diatomite powder is mainly composed of disc-like and cylindrical structures and numerous pores can be clearly seen, indicating the large specific surface area and high porosity of diatomite as expected. However, there are a lot of impurities on the surface of the raw diatomite. Moreover, most of the pores on the surface are blocked by the visible impurities. From Fig. 2(b), it can be clearly observed that after acid treatment there are less impurities and that the pores on the surface of diatomite become more obvious. As seen in Fig. 2(c), the morphology of the porous structure is retained after alkali leaching. Moreover, the clogged pores are dredged in various degrees (Fig. 2(d)). For PEG PCM carrier, it is a good phenomenon because more PEG can be loaded in the pores. SEM technique was also applied to study the morphological changes of diatomite and AgNPs-decorated diatomite (Figs. 2e, f). AgNPs are observed on the surface of diatomite and the porous structure of diatomite remains visible. The energy dispersive X-ray spectroscopy

(EDS) spectrum confirms the presence of silicon (Si), oxygen (O), and silver (Ag) in the composite diatomite. SEM and EDX images confirm that the AgNPs are well dispersed on diatomite.

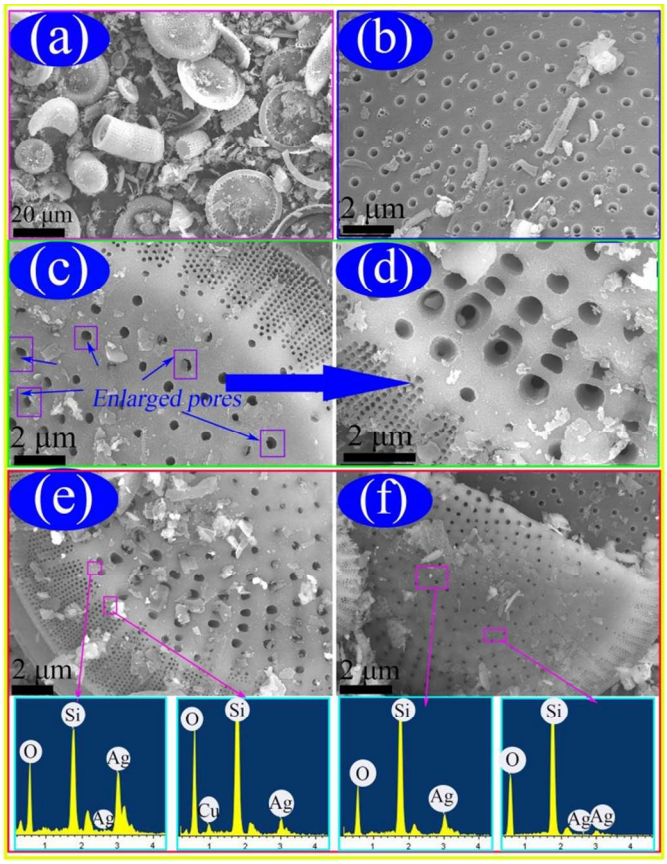

Fig. 2. SEM images of (a) RD; (b) RD-H; (c and d) RD-N; (e and f) DtAg and corresponding EDS analysis.

TEM and EDS analysis. In order to confirm the observations obtained from SEM, TEM was also applied in this study (Fig. 3). In Fig. 3(a), we can clearly observe numerous macropores in the middle region and ordered mesopores in the peripheral area of the diatomite disk, which are in good agreement with the SEM observations. However, most macropores are blocked. In Fig. 3(b), after the treatment with 20 wt.% sulfuric acid, plenty of pores can be clearly seen. Because of the reaction between metallic oxides and sulfuric acid, originally clogged pores are opened and pore edges are enlarged gradually. The changes indicate that metallic oxide is the main stuff which clogs the pore. Since diatomite is mainly composed of SiO_2, the treatment with sodium hydroxide necessarily causes the formation of soluble silicates SiO_3^{2-}. Thus, the larger pores, flaws and cracks are created.[46] As shown in Figs. 3(c) and (d), after the treatment with sodium hydroxide solution, the multi-pore structure of diatomite remains intact and the pores on the surface become larger. Therefore, we conclude that alkali leaching is an effective modification approach to dredge the pores on diatomite. Fig. 3(e) illustrates the TEM image of the AgNPs-decorated diatomite. From Fig. 3(e), most of AgNPs are loaded onto the surface of diatomite instead of into the pores. The energy dispersive X-ray spectroscopy (EDS) spectrum also confirms the presence of silicon (Si), oxygen (O), and silver (Ag) in the composite diatomite. TEM and EDX images confirm that the AgNPs are well dispersed on diatomite.

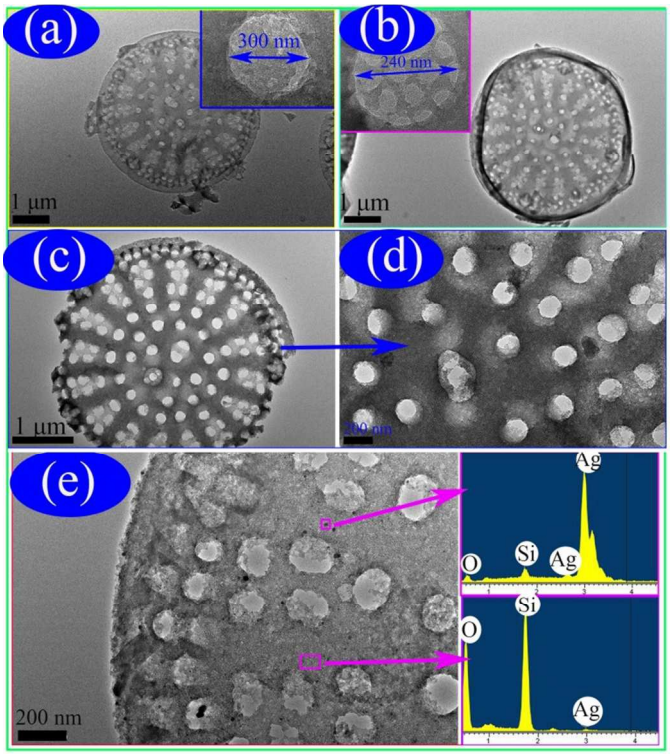

Fig. 3. TEM images of (a) RD; (b) RD-H; (c and d) RD-N; (e) DtAg and corresponding EDS analysis.

HRTEM analysis. The image of AgNPs dispersed on diatomite surface is clearly shown in the high-resolution TEM image (Fig. 4). The AgNPs have spherical shapes with the particle size range of 3~10 nm (Fig. 4a). Fig. 4(b) presents the lattice fringe of the prepared Ag nanoparticles. The lattice fringe of the HRTEM image is examined to be 0.232 nm, close to the (111) lattice spacing of the fcc silver, indicating that the individual particle is also a single crystal.

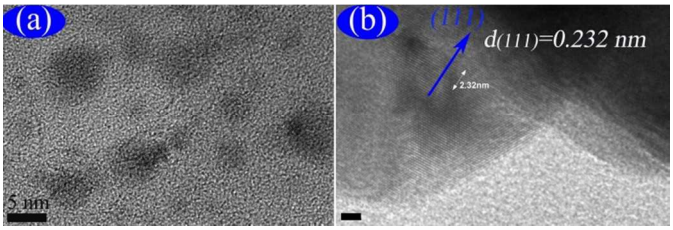

Fig. 4. High-resolution TEM of the AgNPs-decorated on diatomite.

XPS analysis. To further investigate the possible chemical status of Ag element (Ag^0 or Ag^+) in the AgNPs-decorated diatomite powder, the corresponding high-resolution XPS spectrum of Ag 3d5/2 is shown in Fig. 5. The photoelectron peaks of both Ag 3d5/2 and Ag 3d3/2 are basically symmetrical with binding energy of 368.75 and 374.75 eV, respectively, and the splitting of the 3d doublet is 6.0 eV. The result proved that AgNPs certainly existed in the form of metallic Ag. Similar results were also obtained by Ma et al.[47]

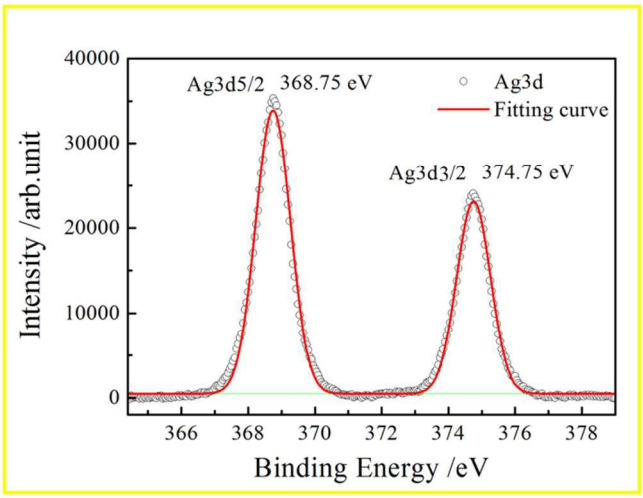

Fig. 5. High-resolution XPS spectrum of Ag 3d in DtAg composite.

Textural properties. The textural properties of diatomite and DtAg powder, as determined by N_2 adsorption-desorption isotherms, were preserved after diatomite grafting with AgNPs. Fig. 6 illustrates the N_2 adsorption–desorption isotherms of diatomite, purified diatomite and DtAg powders, and the results are summarized in Table 2. In Fig. 6(a), the N_2 adsorption–desorption isotherms of all the samples are similar, indicating that the microstructure of the diatomite is maintained after purification and AgNPs decoration. All the N_2 adsorption–desorption isotherms are characterized as a type II isotherm with an H3 hysteresis loop. The hysteresis is associated with the filling and emptying of the mesopores by capillary condensation, indicating the existence of mesopores.[48] Besides, the sharp increase in the N_2 adsorption quantity near the relative pressure of 1 indicates the existence of macropores.[49] Such a feature suggests the co-presence of macropore and mesopore structures, as shown in SEM and TEM images. According to Table 2, after dissolution in alkali solution, three parameters are improved obviously because after the treatment with sodium hydroxide solution, diatomite's pore type has been changed: large pore size is increased and micropore size is reduced, thus resulting in the increase in the surface area. After AgNPs decoration, three parameters decrease, but the values are still larger than those of the raw diatomite. Pore size distribution (PSD) is another valuable factor. Concerning the pore size distribution in Fig. 6(b), the pore size distributions of all the diatomite materials show a similar narrow range of 5–10 nm. We noted that the typical pore size distribution of AgNPs decorated diatomite was comparable to the raw diatomite, which was desirable for its role as PCM carrier.

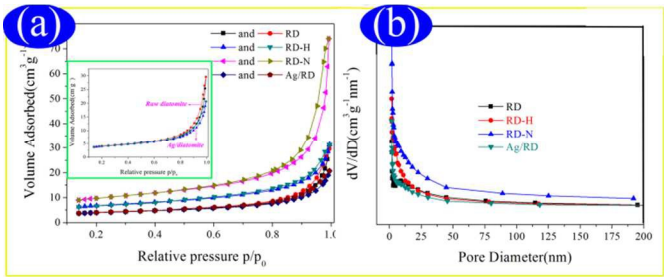

Fig. 6. N_2 adsorption–desorption isotherms and pore size distributions of raw, purified, and AgNPs-decorated diatomite.

Table 2 Textural properties of raw diatomite, purified diatomite, and AgNPs decorated diatomite

Results	Samples			
	RD	RD-H	RD-N	DtAg
Specific surface area (m^2/g)	13.8021	24.0548	29.8761	14.0290
Pore volume (cc/g)	0.0241	0.0362	0.0649	0.0297
Mean Pore Diameter (nm)	6.02	8.18	9.47	6.7832

Analysis of the prepared PEG/DtAg ss-PCMs

Chemical compatibility analysis. Chemical compatibility between PEG and DtAg was determined via XRD and FT-IR analysis. Fig. 7 shows the XRD patterns of diatomite, DtAg and the prepared PEG/DtAg ss-PCM. As shown in Fig. 7(a), the diatomite has the typical non-crystalline diffraction peaks of SiO_2. A significant amount of quartz crystalline phase is also found. As seen in Fig. 7(b), all strong patterns can be indexed as the pure Ag. The result is well consistent with the reported data (JCPDS87-0718). No other pattern can be observed and the diffraction peaks of the samples are sharp and narrow, indicating the high purity of the as-prepared AgNPs. In Fig. 7(c), the peaks at 19° and 23° are assigned to PEG crystal. It can be clearly seen that all the sharp and intense diffraction peaks of PEG are observed for the prepared PEG/DtAg composite, indicating that the crystal structure of PEG is not destroyed after impregnation.

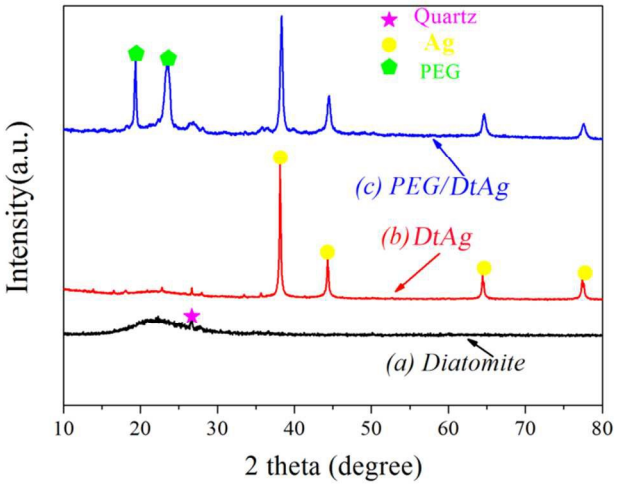

Fig. 7. XRD patterns of diatomite, PEG and the prepared PEG/DtAg ss-PCM.

Fig. 8 demonstrates the FT-IR spectra of PEG, DtAg, and composite PCM. In Fig. 8(a), the typical stretching vibrations of C–H at 964 and 2888 cm^{-1} correspond to $–CH_2$ of PEG. Moreover, the stretching vibrations of C–O and –OH are observed at 1109 and 3444 cm^{-1}, respectively. In Fig. 8(b), peaks 1107 and 807 cm^{-1} are respectively caused by Si–O–Si asymmetry stretching vibration and the Si–O–Si symmetric stretching vibration. The peak at 466 cm^{-1} can be assigned to the Si–O–Si bending vibration. In addition, the stretching vibration and the bending vibration of OH functional group are found at the wavenumber of 3446 and 1637 cm^{-1}, respectively. All these characteristic peaks suggest that diatomite is mainly composed

of SiO_2. Besides, no peak is observed near 530 cm^{-1}, indicating that Ag in the composite material is in the form of pure silver.[50] In Fig. 8(c), we can observe that all the typical peaks of PEG are shown in the spectrum of composite PCM, such as C–H stretching vibration (964 and 2888 cm^{-1}), C–O vibration (1109 cm^{-1}), and –OH vibration (3444 cm^{-1}). The primary diatomite functional groups are also found in the spectrum of composite PCM. There is no significant new peak, indicating that there is no chemical interaction between PEG and DtAg.

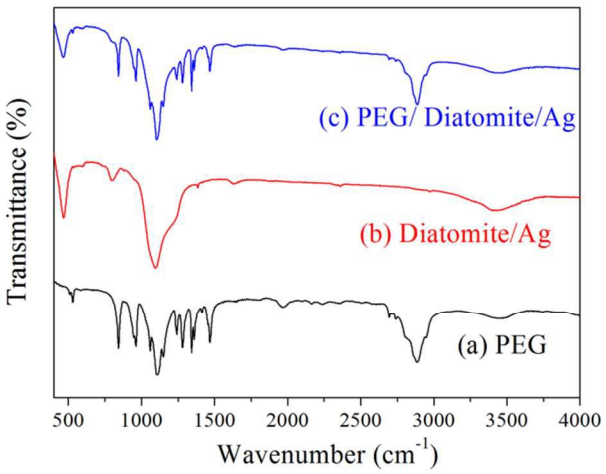

Fig. 8. FTIR spectra of diatomite, PEG and the prepared PEG/DtAg ss-PCM.

Micro-morphology analysis. Fig. 9 shows that PEG with different mass ratios (30%, 40%, 50%, and 63%) is well dispersed in the porous structure of the DtAg. The multi-porous structure of the diatomite prevented the leakage of liquid PEG because of the capillary action and surface tension force. As shown in Fig. 9(d), PEG is not leaked from the surface of the composite when the PEG is in the melting state because the hot spot made by the electric beam makes the investigated PCM locally melt when conducting SEM. Therefore, the maximum appropriate mass ratio of the PEG in the composites was determined as 63%.

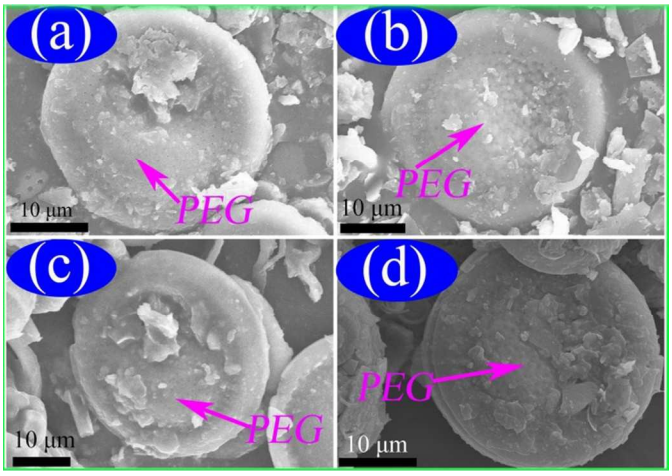

Fig. 9. SEM images of the prepared PEG/DtAg ss-PCMs.

TEM was also performed to evaluate the morphology of materials. Fig. 10 illustrates the TEM images of the composite PCMs prepared with different PEG mass ratios (30%~63%). Similar to the SEM results, PEG is well dispersed into the pore structure of supporting diatomite, which provides the good mechanical strength for the whole composite and prevents the leakage of the melted PEG. Different form SEM results, we can see a uniform distribution of AgNPs on the surface of diatomite, which is beneficial for the improvement of thermal conductivity. The AgNPs have the spherical shape with the particle size range of 3~10 nm. In this experiment, the maximum mass percentage of the PEG in the composites was determined to be 63%. PEG is not leaked from the composites even when the PEG in the composites melts.

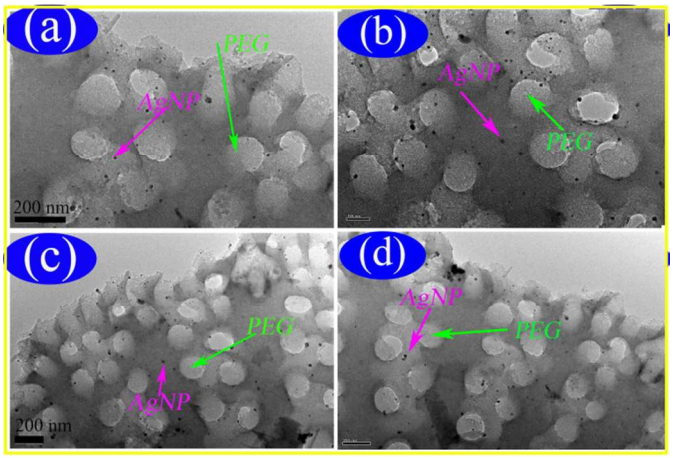

Fig. 10. TEM images of the prepared PEG/DtAg ss-PCMs.

Phase change behavior of the prepared PEG/DtAg ss-PCMs

Thermal properties including thermal energy storage capacity and phase changing temperature can be determined by means of DSC technique. The phase change parameters of all the prepared composite PCMs are summarized in Table 3. As a critical factor for PCMs, phase change enthalpy is always considered as the most reliable indicator for evaluating the thermal energy storage capacity of the prepared composite PCMs. Because the supporting DtAg does not undergo a phase transition process and it is the PEG that accounts for the latent thermal heat, the latent heat increases with the increase of the mass fraction of PEG. According to Table 3, ss-PCM4 can be unquestionably considered as the most promising latent heat storage material. Fig. 11(a) demonstrates the melting and solidifying DSC curve of ss-PCM4 composite. The DSC curves of other composite PCMs are similar. The DSC results suggest that the ss-PCM4 while undergoing cyclic freezing and melting processes has exhibited only single peak, which conforms to the liquid-to-solid phase transition and vice versa respectively. It is found from Fig. 11(a) that the optimal PEG/DtAg ss-PCM freezes at 41.02 ^{o}C with a latent heat of 102.4 J/g and melts at 59.45 ^{o}C with a latent heat of 111.3 J/g when the adsorption ratio of the PEG is 63%.

The theoretical enthalpy of ss-PCM can be determined by Eq. (1):[51]

$$H_{Theo} = \eta \cdot H_{PEG}, \quad (1)$$

where H_{Theo} is the theoretical enthalpy of prepared the ss-PCM; η is the mass fraction of the PEG in composite PCMs; H_{PEG} denotes the enthalpy of pristine PEG. The theoretical and actual enthalpies of the prepared ss-PCMs are shown in Fig. 11(b). We found that the actual enthalpies of ss-PCMs were slightly lower than their corresponding theoretical values. The difference may be interpreted as follows: the drag and steric effects of nano- and meso-pores restrict the crystal arrangement and orientation of PEG molecular chains, resulting in the decline of regularities of crystal line regions and the increase of lattice defects. Similar results were reported by Feng et al.[52]

Moreover, the melting enthalpy is always larger than their freezing enthalpy. This may be caused by the fact that mass loss increases when the composite is heated from 20 to 80 °C during melting test by the DSC. Thereafter, the freezing test is conducted. Due to the mass loss of PEG/DtAg in the melting test, the freezing enthalpy of is smaller in the solidifying test.

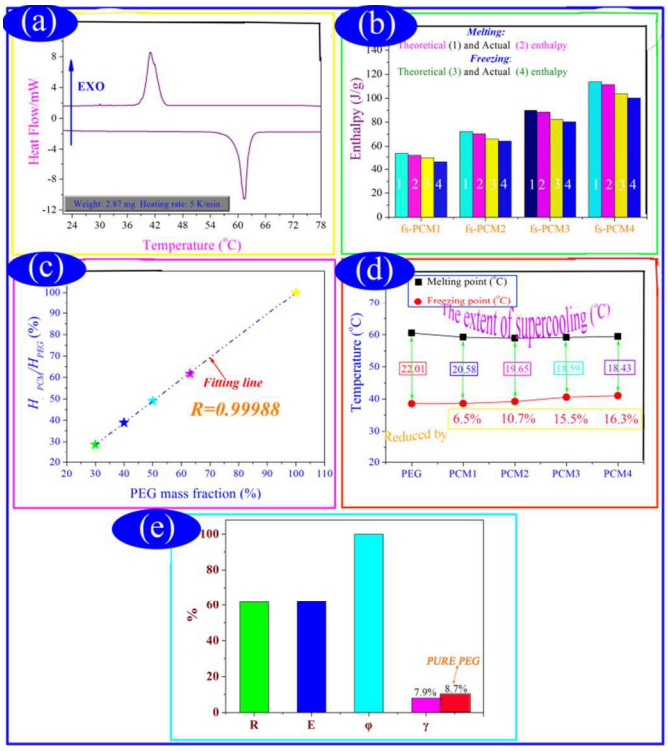

Fig. 11. PEG and ss-PCMs: (a) DSC curves of ss-PCM4; (b) comparison of theoretical and actual enthalpies; (c) the relation between the PEG mass fraction and Hss-PCM/HPEG; (d) Phase change temperatures; (e) Thermal characteristics.

According to the relation between the PEG mass fraction and $H_{ss\text{-}PCM}/H_{PEG}$ of the samples (Fig. 11(c)), the phase change enthalpy of the composite materials is linearly correlated with the loading of PEG in the concentration range in our experiment.

The extent of supercoiling can be determined as the difference between the melting and freezing temperature and the corresponding evaluation results are illustrated in Fig. 11(d). The supercooling extents of the prepared ss-PCM1, ss-PCM2, ss-PCM3, and ss-PCM4 are respectively 6.5%, 10.7%, 15.5%, and 16.3% lower than that of the pristine PEG. The result suggests that the supercooling extent of PEG can be favorably reduced by impregnation with DtAg substrate. Besides, the melting temperature of the ss-PCMs is lower than that of the pristine PEG, while the freezing temperature of the ss-PCMs is higher than that of the pristine PEG (Fig. 11(d)). The reason is that the porous DtAg network in the composites can provide heat conduction path in the PEG and consequently accelerate the phase change speed of the composites. In other words, the heat at the outer side of the composite PCMs can be transferred to the inner side more easily due to the thermal conductivity enhancement of AgNPs, which results in the faster melting of the sample and vice versa in the freezing process. Without AgNPs, PEG/diatomite was also prepared and denoted as ss-PCM5. Its thermal parameters are shown in Table 3. The supercooling extent is 10% higher than that of PEG/DtAg. Factually, the cold energy provided by the heat transfer fluid was transferred to the PEG, indicating the presence of the dispersed AgNPs in the composite PCM. In this way, the supercooling extent was obviously reduced.[53]

Table 3 Thermal characteristics of PEG and the prepared PEG/DtAg ss-PCMs

Samples	PEG Mass Ratio (wt%)	Melting Process		Solidifying Process	
		H_M(J/g)	T_M(°C)	H_S(J/g)	T_S(°C)
PEG PCM	100	180.3	60.51	164.6	38.5
ss-PCM1	30	51.5	59.21	46.1	38.63
ss-PCM2	40	70.2	58.86	64.1	39.21
ss-PCM3	50	88.4	59.13	80.3	40.54
ss-PCM4	63	111.3	59.45	102.4	41.02
ss-PCM5	63	110.7	59.83	103.3	39.54

Four important parameters, including the impregnation ratio (R), impregnation efficiency (E), thermal storage capability (φ) and heat storage efficiency (γ), were employed to characterize the phase change performance of the prepared PEG/DtAg ss-PCM4,[54] and can be calculated by the following four equations:

$$R = \frac{H_{M,com}}{H_{M,PEG}} \times 100\%, \quad (2)$$

$$E = \frac{H_{M,com} + H_{F,com}}{H_{M,PEG} + H_{F,PEG}} \times 100\%, \quad (3)$$

$$\varphi = \frac{\frac{H_{M,com} + H_{F,com}}{R}}{H_{M,PEG} + H_{F,PEG}} \times 100\%, \quad (4)$$

$$\gamma = \left(1 - \frac{H_{F,com}}{H_{M,com}}\right) \times 100\%, \quad (5)$$

where $H_{M,com}$ and $H_{F,com}$ are the melting and freezing phase change enthalpies, respectively; $H_{M,PEG}$ and $H_{F,PEG}$ respectively represent the melting latent heat and freezing latent heat of PEG. The calculated results of R, E, φ, and γ of ss-PCM4 samples are shown in Fig. 11(e). The ss-PCM4 achieved the impregnation ratio of 61.7% and the impregnation efficiency of 62% at the PEG/DtAg mass ratio of 63/37. However, these two values are lower than the theoretical PEG mass ratio. In fact, R indicates the effective impregnation of PEG within the structure of DtAg substrate, while E describes an effective performance of the PEG inside the composite for latent heat storage. Considering that the phase change hardly occurs upon the PEG inside the tiny pores due to the confinement effect on molecule motion. All the PEG could not actually serve as PCMs. Interestingly, the thermal storage capability of the prepared ss-PCM4 is chose to 100%, indicating that almost all PEG molecule chains could effectively store/release heat through phase change. Moreover, from Fig. 11(e), we can also observe that the heat loss percentage of pure PEG between endothermic and exothermic cycles is 9% higher than that of the composite ss-PCM4.

Thermal stability of the prepared PEG/DtAg ss-PCM

Thermal stability is a significant evaluation indicator of the composite PCMs for the applications of heat energy storage or thermal regulation. Fig. 12 displays TGA curves and DTG thermograms of the composite PCM. The weight loss profile of the ss-PCM4 was quite similar to those in our previous studies[12,13] and its thermal decomposition was performed in the programmed temperature range of 350–450 °C through a one-step degradation.

Corresponding to the degradation process, the sharp weight loss at 393 °C can be ascribed to the decomposition of organic ingredients, namely, the breaking of the PEG chains. Thus, the composite PCM has superior thermal stability within its working temperature range because the degradation of PEG occurs at 367 °C. Moreover, the composite has the residue of 37.9 wt.% at 600 °C, suggesting that the prepared PEG/DtAg ss-PCM is homogeneous. According to the DSC measurement results, the impregnation ratio of PEG was calculated to be 61.7%, which was slightly lower than the loading content (62.1%) of PEG in the composite.

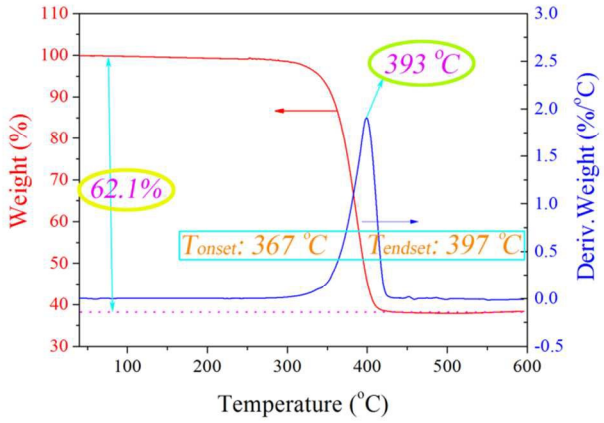

Fig. 12. TGA curve and corresponding DTG thermogram of PEG/DtAg ss-PCM.

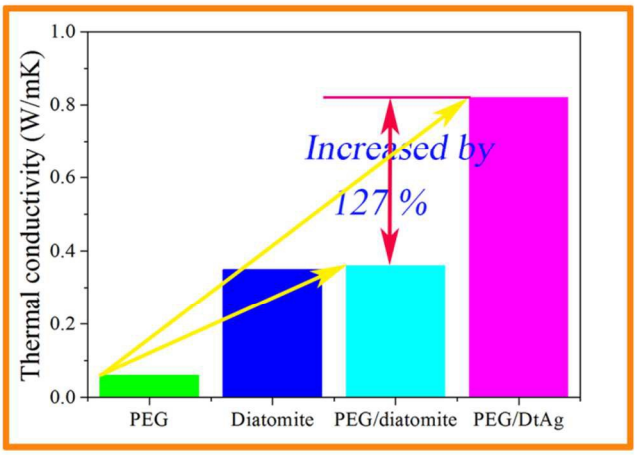

Fig. 13. Thermal conductivity of the samples.

Thermal performance of the prepared PEG/DtAg ss-PCM

Thermal conductivity improvement. Thermal conductivity measurement was conducted with a hot disk thermal constants analyzer at room temperature. According to the thermal conductivities of PEG, diatomite, PEG/diatomite, and PEG/DtAg (Fig. 13), the thermal conductivity of the final ss-PCM has been obviously improved through a "two-step process". The significantly improved thermal conductivity was firstly observed when the PEG was impregnated into diatomite pores due to the relatively high thermal conductivity of diatomite itself. It is well known that metallic silver had a particularly high thermal conductivity, 429 $W \cdot m^{-1} \cdot K^{-1}$. The thermal conductivity of PEG/DtAg ss-PCM can be improved by AgNPs doping. After AgNPs doping, the value was further increased by 127% as expected. The results indicated that when AgNPs were homogeneously dispersed into the ss-PCM, they improved the thermal conductivity of the composite PCM and consequently enhanced heat transfer.

Melting and freezing characteristics. The improvement of the thermal conductivity was also verified by comparing the melting and freezing performances of PEG/DtAg with those of the PEG/diatomite composite. Temperature curves for melting and freezing processes of the composite PCMs with or without AgNPs are shown in Fig. 14. The melting time was estimated as the period from the same initial temperature (25 °C) to the over-melting point of the PCM (60 °C). Similarly, the freezing time was determined as the period from the same initial temperature (60 °C) to the melting point of the PCM (25 °C). The detailed operation was given in the *Supporting Information*. As shown in Fig. 14, the melting periods of PEG/diatomite and PEG/DtAg composites are respectively 50 min and 33 min. The freezing periods of PEG/diatomite and PEG/DtAg composites are respectively 40 min and 30 min. The decreased melting and freezing periods of PEG/DtAg compared with those of the PEG/diatomite may be attributed to the increase in the heat transfer rate during heating and cooling periods. These results indicated that the heat transfer rate in the composite PCM with AgNPs additive was higher than that of the composite PCM without AgNPs additive.

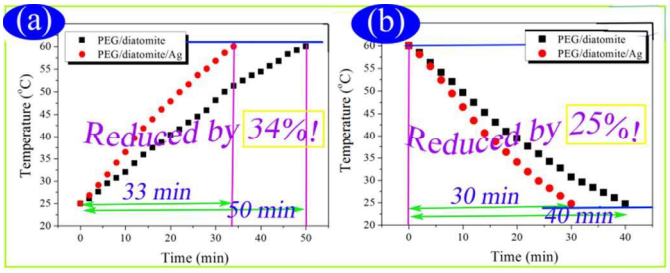

Fig. 14. Melting and freezing process curves of PEG/diatomite and PEG/DtAg ss-PCMs.

Thermal reliability of the prepared PEG/DtAg ss-PCMs

The prepared composite PCM should be stable in terms of chemical and thermal manners over a large number of melting and freezing cycling. In other words, the shape-stabilized composite PCM should show no or little change in the chemical structure or thermal properties after the long-term service period. Therefore, a 200-thermal cycling test was performed to determine the change in chemical structure and thermal properties of the shape-stabilized PEG/DtAg composite PCM. After numerous melting and freezing cycles, no seepage of melted PEG was found.

Chemical structure analysis. Fig. 15(a) shows the SEM photographs of PEG/DtAg after thermal cycling experiment. In Fig. 15(a), the morphology of the disc structure is intact. PEG is fully dispersed into diatomite pores and nearly no empty pore has been found. The XRD analysis of the composite PCM before and after thermal treatment is presented in Fig. 15(b). No obvious difference could be found between the two diffraction peaks, suggesting that the crystal structure of PEG in the shape-stabilized composite PCM was not affected by thermal cycling and that the chemical degradation did not occur during the thermal cycling process. The FT-IR spectra of the shape-stabilized composite PCM before and after thermal cycling are shown in Fig. 15(c). The shapes or frequency values of all the peaks were not changed after thermal cycling. Thus, it can be concluded that the chemical structure of the shape-stabilized composite PCM was not impaired by repeated

melting and freezing cycling. Therefore, it is worth mentioning that the shape-stabilized composite PCM is chemically stable after 200 thermal cycles.

Thermal behavior analysis. Fig. 15(d) shows the DSC curves of the shape-stabilized composite PCM before and after thermal cycling. After 200 thermal cycles, the melting temperature of composite PCM was changed by 0.29 ^{o}C. The changes in melting temperatures with the increase in the number of thermal cycles are not in the significant magnitude for TES applications. Besides, the melting latent heat value of the composite PCM was changed by 1.3%. As the changes in the phase change temperature and latent heat storage of the composite PCM are small, it can be deduced that the shape-stabilized composite PCM has good thermal reliability and can be used as heat energy storage material in buildings.

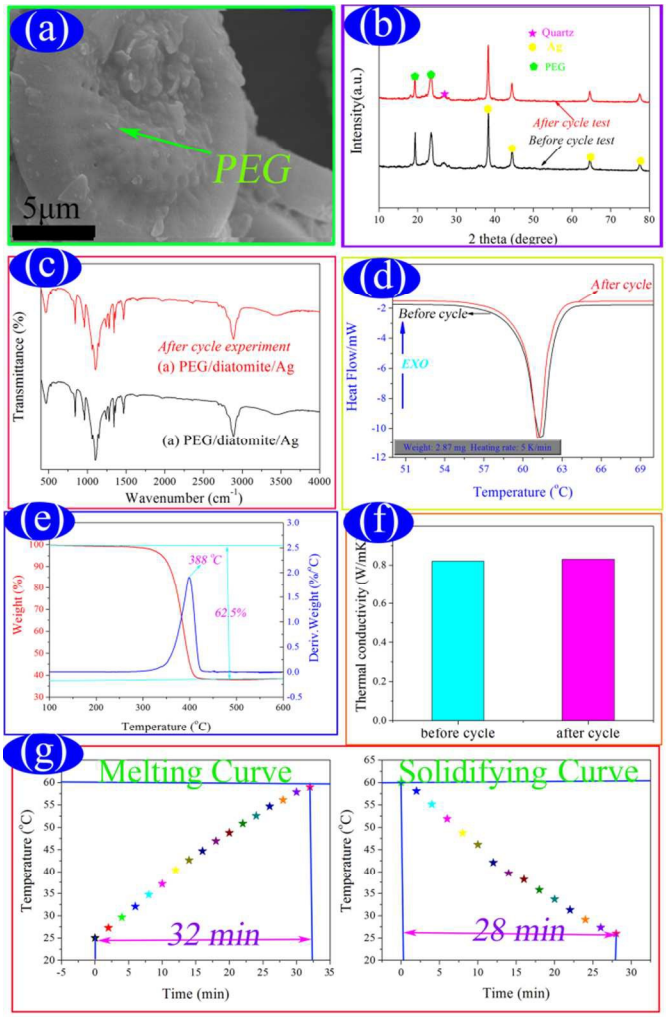

Fig. 15. The ss-PCM4 after 200 cycles: (a) SEM image; (b) XRD analysis; (c) FTIR spectra; (d) DSC curves; (e) TGA curve and the corresponding DTG thermogram; (f) Thermal conductivity measurement; (g) Melting and freezing process curves.

Fig. 15(e) illustrates the TGA curve and DTG thermogram of the composite PCM after thermal cycling. In Fig. 15(e), the degradation of PEG occurs at 380 ^{o}C. The result showed that the composite PCM has good thermal stability even after the thermal cycling. Besides, the residue reached 37.5 wt.%, which was well consistent with the corresponding DSC analysis.

Fig. 15(f) shows the comparison results of the thermal conductivity measurements of composite PCM before and after cycle test. No obvious difference was observed. Fig. 15(g) displays the melting and freezing process curves of the composite PCM after thermal cycling. In Fig. 15(e), the melting and freezing periods are respectively 32 min and 28 min. After thermal cycling, the melting and freezing periods were changed by 2 min. The change was quite beneficial for the industrial applications.

Conclusion

A series of high thermal-conductive PEG/DtAg shape-stabilized composite PCMs were prepared via vacuum impregnation operation. Our study capitalized on the high thermal conductivity of AgNPs. Raw diatomite was treated by the alkali-leaching method to dig its pores. Based on the above discussion, the conclusions can be drawn as follows:

(1) With alkali-leaching diatomite, the maximum load of PEG in the composite ss-PCM could reach 63 wt.%, which was 31% higher than that of the raw diatomite. The 5-min alkali treatment (5%, 80 ^{o}C) could dredge and enlarge the pores, thus leading to the higher BET area and the higher pore size and changing the overall morphology.

(2) Spherical-shaped crystalline AgNPs with the diameter range of 3~10 nm were uniformly decorated onto the diatomite (SEM, HRSEM, EDS and XPS results). For the addition proportion of 7.2 wt,% Ag in PEG/diatomite PCM, the thermal conductivity was 0.82 $W \cdot m^{-1} \cdot K^{-1}$, which was enhanced by 127% compared to PEG/diatomite composite. The reduced melting and freezing time indirectly proved the results. These values remain unchanged even after a 200-cycle test.

(3) The resulting 63%PEG/DtAg ss-PCM owns the high exudation stability even in the liquid state of PEG. The DSC results indicated that the ss-PCM was melted at 59.45 ^{o}C with a latent heat of 111.3 J/g and solidified at 41.02 ^{o}C with a latent heat of 102.4 J/g. SEM and TEM results indicated that PEG was well impregnated. XRD, FT-IR, TGA and 200-cycle test results proved the excellent chemical compatibility and the improved supercooling extent, stability, and reliability.

Acknowledgements

This project was supported by the program for New Century Excellent Talents in University (Grant No. NCET-08-828), the program for the Excellent Adviser (Grant No. 53200959641), and the Fundamental Research Funds for the Central Universities (Grant No. 2011YXL003, 53200959396 and 53200959775).

Notes and references

† **Corresponding author:** Jinhong Li, E-mail: jinhong@cugb.edu.cn.
Address: School of Materials Science and Technology, Beijing Key Laboratory of Materials Utilization of Nonmetallic Minerals and Solid Wastes, National Laboratory of Mineral Materials, China University of Geosciences (Beijing), Beijing, 100083, China.

Electronic Supplementary Information (ESI) available: See DOI: 10.1039/b000000x/

[1] A. Pasupathy, R. Velraj, and R.V. Seeniraj, Renew. Sustain. Energy Rev., 2008, **12**, 39–64.
[2] R. Baetens, B.P. Jelle, and A. Gustavsend, Energy Build., 2010, **42**, 1361–1368.

[3] Y.M. Wang, B.T. Tang, and S.F. Zhang, J. Mater. Chem., 2012, **22**, 18145–18150.
[4] M. Sokolov and Y. Keizman, Sol. Energy, 1991, **47**, 339–346.
[5] S. Mondal, Appl. Therm. Eng., 2008, **28**, 1536–1550.
[6] Q.H. Meng and J.L. Hu, Sol. Energy Mater. Sol. C., 2008, **92**, 1260–1268.
[7] N. Sarier and E. Onder, Thermochim. Acta, 2012, **540**, 7–60.
[8] D. Rozanna, A. Salmiah, T.G. Chuah, R. Medyan, S.Y.T. Choong, and M. Sa'ari, J. Oil Palm Res., 2005, **17**, 41–46.
[9] N.A.M. Amin, F. Bruno, and M. Belusko, Appl. Energy, 2014, **122**, 280–287.
[10] S. Jegadheeswaran and S.D. Pohekar, Renew. Sustain. Energy Rev., 2009, **13**, 2225–2244.
[11] S. Karaman, A. Karaipekli, A. Sarı, and A. Biçer, Sol. Energy Mater. Sol. C., 2011, **95**, 1647–1653.
[12] T.T Qian, J.H. Li, H.W. Ma, and J. Yang, Polym. Compos., In press (DOI: 10.1002/pc.23243).
[13] T.T Qian, J.H. Li, H.W. Ma, and J. Yang, Sol. Energy Mater. Sol. C., 2015, **132**, 29–39.
[14] A.A. Ahmet, Chem. Eng. J., 2013, **231**, 477–483.
[15] M.N.A. Hawlader, M.S. Uddin, and M.M. Khin, Appl. Energy, 2003, **74**, 195–202.
[16] A. Mallow, O Abdelaziz, K Kalaitzidou, and S Graham, J. Mater. Chem., 2012, **22**, 24469–24476.
[17] S.D. Zhang, Q.H. Tao, Z.Y. Wang, and Z.P. Zhang, J. Mater. Chem., 2012, **22**, 20166–20169.
[18] D. Zhang, J. Zhou, K. Wu, and Z.J. Li, Sol. Energy, 2005, **78**, 351–480.
[19] A. Sarı, A. Karaipekli, and K. Kaygusuz, Int. J. Energy Res., 2008, **32**, 154–160.
[20] D. Zhang, Z. Li, J. Zhou, and K. Wu, Cement. Concrete. Res., 2004, **34**, 927–934.
[21] C. Jiao, B. Ji, and D. Fang, Mater. Lett., 2012, **67**, 352–354.
[22] A. Karaipekli and A. Sarı, Renew. Energy, 2008, **33**, 2599–2605.
[23] A. Karaipekli and A. Sarı, Sol. Energy, 2009, **83**, 323–332.
[24] A. Sarı and A. Biçer, Sol. Energy Mater. Sol. C., 2012, **101**, 114–122.
[25] Z.M. Sun, Y.Z. Zhang, S.L. Zheng, Y. Park, and R.L. Frost, Thermochim. Acta, 2013, **558**, 16–21.
[26] M. Li, Z. Wu, H. Kao, and J. Tan, Energy Convers. Manage., 2011, **52**, 3275–3281.
[27] C.Z. Chen, X.D. Liu, W.M. Liu, and M.F. Ma, Sol. Energy Mater. Sol. C., 2014, 127, 14–20.
[28] X.M. Fang, Z.G. Zhang, and Z.H. Chen, Energy Convers. Manage., 2008, **49**, 718–723.
[29] M. Li, Z.S. Wu, and H.T. Kao, Appl. Energy, 2011, **88**, 3125–3132.
[30] S.K. Song, L.J. Dong, Y. Zhang, S. Chen, Q. Li, Y. Guo, S.F. Deng, S. Si, and C.X. Xiong, Energy, 2014, **76**, 385–389.
[31] S.Y. Liu, and H.M. Yang, Appl. Clay Sci., 2014, **101**, 277–281.
[32] S.A. Memon, T.Y. Lo, X. Shi, S. Barbhuiya, and H.Z. Cui, Appl. Therm. Eng., 2013, **59**, 336–347.
[33] Z.M. Sun, W.A. Kong, S.L. Zheng, and R.L. Frost, Sol. Energy Mater. Sol. C., 2013, **117**, 400–407.
[34] D.D. Mei, B. Zhang, R.C. Liu, Y.T. Zhang, and J.D. Liu, Sol. Energy Mater. Sol. C., 2011, **95**, 2772–2777.
[35] H. Hadjar, B. Hamdi, M. Jaber, J. Brendle, Z. Kessaissia, H. Balard, and J.B. Donnet, Micropor. Mesopor. Mat., 2008, **107**, 219–226.
[36] E. Li, X.Y. Zeng, and Y.H. Fan, Desalination, 2009, **238**, 158–165.
[37] K.W. Jung, D. Jang, and K.H. Ahn, Int. J. Miner. Process., 2014, **131**, 7–11.
[38] Z.M. Sun, X.P. Yang, G.X. Zhang, S.L. Zheng, and R.L. Frost, Int. J. Miner. Process., 2013, **125**, 18–26.
[39] S. Jegadheeswaran and S.D. Pohekar, Renew. Sustain. Energy Rev., 2009, **13**, 2225–2244.
[40] A. Elgafy and K. Lafdi, Carbon, 2005, **43**, 3067–3074.
[41] B.T. Tang, M.G. Qiu, and S.F. Zhang, Sol. Energy Mater. Sol. C., 2012, **105**, 242–248.
[42] Y.M. Wang, B.T. Tang, and S.F.Zhang, Adv. Funct. Mater., 2013, **23**, 4354–4360.
[43] B.T. Tang, Y.M. Wang, M.G. Qiu, S.F. Zhang, Sol. Energy Mater. Sol. C., 2014, **123**, 7–12.
[44] S.N. Schiffres, S. Harish, S. Maruyama, J. Shiomi, J.A. Malen, ACS nano, 2013, **7**, 11183–11189.
[45] W.L. Wang, X.X. Yang, Y.T. Fang, J. Ding, and J.Y. Yan, Appl. Energy, 2009, 86, 1196–1200.
[46] J. Zhang, Q.W. Ping, M.H. Niu, H.Q. Shi, and N. Li, Appl. Clay Sci., 2013, **12–16**, 83–84.
[47] J.Q. Ma, X.H. Guo, Y.Y. Zhang, and H.G. Ge, Chem. Eng. J., 2014, **258**, 247–253.
[48] W.B. Yu, P. Yuan, D. Liu, L.L. Deng, W.W. Yuan, B. Tao, H.F. Cheng, and F.R. Chen, J. Hazard. Mater., 2015, **285**, 173–181.
[49] D. Liu, P. Yuan, D. Tan, H. Liu, T. Wang, M. Fan, J. Zhu, and H. He, J. Colloid Interface Sci., 2012, **388**, 176–184.
[50] G.I.N. Waterhouse, G.A. Bowmaker, and J.B. Metson, Phys. Chem. Chem. Phys., 2001, **3**, 3838.
[51] Y. Qian, P. Wei, P.K. Jiang, Z. Li, Y.G. Yan, and J.P. Liu, Appl. Energy, 2013, **106**, 321–327.
[52] L.L. Feng, W. Zhao, J. Zheng, S. Frisco, P. Song, and X.G. Li, Sol. Energy Mater. Sol. C., 2011, **95**, 3550–3556.
[53] R. Parameshwaran, R. Jayavel, and S. Kalaiselvam, J. Therm. Anal. Calorim., 2013, **114**, 845–858.
[54] S.Y. Yu, X.D. Wang, and D.Z. Wu, Appl. Energy, 2014, **114**, 632–643.

Graphical Abstract

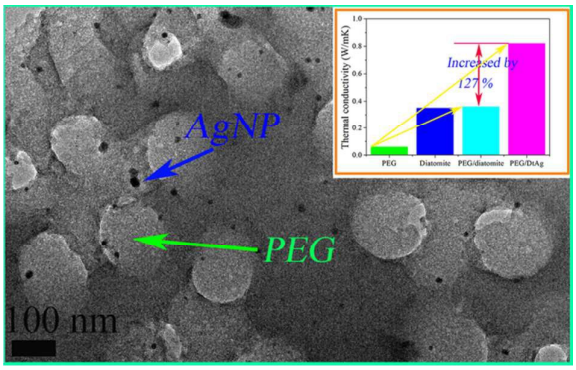

Thermal conductivity was 0.82 $W \cdot m^{-1} \cdot K^{-1}$ for 7.2% AgNP in PEG/diatomite, which was enhanced by 127% compared to PEG/diatomite.